High Power Laser Science and Engineering, (2022), Vol. 10, e46, 7 pages.
doi:10.1017/hpl.2022.38

HIGH POWER LASER SCIENCE AND ENGINEERING

RESEARCH ARTICLE

Intense harmonic generation driven by a relativistic spatiotemporal vortex beam

Lingang Zhang[1], Liangliang Ji[1], and Baifei Shen[2]

[1] *State Key Laboratory of High Field Laser Physics and CAS Center for Excellence in Ultra-intense Laser Science, Shanghai Institute of Optics and Fine Mechanics, Chinese Academy of Sciences, Shanghai, China*

[2] *Department of Physics, Shanghai Normal University, Shanghai, China*

(Received 10 October 2022; revised 11 November 2022; accepted 23 November 2022)

Abstract

Spatiotemporal optical vortex (STOV) pulses carrying purely transverse intrinsic orbital angular momentum (TOAM) are attracting increasing attention because the TOAM provides a new degree of freedom to characterize light–matter interactions. In this paper, using particle-in-cell simulations, we present spatiotemporal high-harmonic generation in the relativistic region, driven by an intense STOV beam impinging on a plasma target. It is shown that the plasma surface acts as a spatial–temporal-coupled relativistic oscillating mirror with various frequencies. The spatiotemporal features are satisfactorily transferred to the harmonics such that the TOAM scales with the harmonic order. Benefitting from the ultrahigh damage threshold of the plasma over the optical media, the intensity of the harmonics can reach the relativistic region. This study provides a new approach for generating intense spatiotemporal extreme ultraviolet vortices and investigating STOV light–matter interactions at relativistic intensities.

Keywords: high-order harmonic generation; relativistic laser–plasma interaction; spatiotemporal optical vortex; transverse orbital angular momentum

1. Introduction

Angular momenta (spin or orbital) are recognized as critical light characteristics. The spin angular momentum (SAM, $\pm\hbar$ per photon) is associated with the circularly polarized state of photons[1], whereas the orbital angular momentum (OAM) originates from the helical wavefront of optical vortices[2], typified by the Laguerre–Gaussian (LG) beam[3]. The LG beam has a spiral phase of the form $\exp(il\phi)$, where l is the topological charge and ϕ is the azimuthal angle in the transverse plane. Such a phase possesses a purely spatial singularity and provides the beam with a donut intensity distribution and an integrated longitudinal OAM ($l\hbar$ per photon, where $\hbar$ is the reduced Planck's constant) parallel to its propagation direction. In the past three decades, these spatial vortices carrying longitudinal OAM have attracted significant interest for multidisciplinary applications (see Refs. [4, 5] and the references cited there).

Concurrent with progress in high-power lasers[6,7], the production of intense spatial vortex beams in the relativistic region ($> 10^{18}$ W cm^{-2} for a laser wavelength of ~ 1 μm) has been theoretically proposed[8–10] and demonstrated in laboratories[11–13]. Such advanced light sources provide new possibilities for light–matter interactions, such as donut/twist wakefield acceleration[14–16], attosecond electron bunch generation[17–19], formation of a large magnetic field[20], high-harmonic generation (HHG)[12,21,22] and the spin–orbital interaction[23–27]. In particular, the SAM and/or OAM of fundamental-frequency photons are transferred into high harmonics during HHG. Thus, it provides a fundamental approach for producing intense ultrafast optical vortices in the extreme ultraviolet (EUV) region.

Apart from longitudinal OAM, theoretical predictions[28,29] and recent experiments[30–32] indicate that light can possess a new class of OAM, tilted or orthogonal to the propagation direction, that is, transverse intrinsic orbital angular momentum (TOAM). In contrast to the conventional spatial vortex beam, such light-carrying TOAM is essentially polychromatic with phase singularity in the spatiotemporal domain, known as the spatiotemporal optical vortex (STOV)[33–35]. Recently, investigations have shown that TOAM can be broadly incorporated into cylindrical vector[36], partially temporally coherent[37], diffraction-free Bessel[38] and traditional spatial vortex beams. In the latter cases, a spatiotemporal wavepacket with orientation-controllable OAM[39–41] can be produced

Correspondence to: L. Ji, Shanghai Institute of Optics and Fine Mechanics, Chinese Academy of Sciences, Shanghai 201800, China. Email: jill@siom.ac.cn. B. Shen, Shanghai Normal University, Shanghai 200234, China. Email: bfshen@shnu.edu.cn

by assembling TOAM and longitudinal OAM, which may be applied in optical spanners with arbitrary three-dimensional orientation.

Accordingly, the interaction of such STOV pulses with matter has been investigated. Novel types of transverse pulse shifts and time delays can be induced when an STOV beam is reflected and refracted at a planar interface[42], which differs from the spatial deflection effect related to spatial vortices[43,44]. The generation of high harmonics carrying TOAM has also been reported, with beta-barium borate crystals[45,46] and gaseous targets[47] as conversion media. However, the STOV beams involved are restricted to low intensities, considering the limitations of the media damage thresholds. Very recent studies have demonstrated that STOV beams could be focused on subwavelength spatial sizes and femtosecond pulse durations[48,49], exhibiting the ability to yield high-intensity STOV pulses. In addition, they can be produced through the coherent beam combing technique that superposes intense plane waves with different wavevectors. Other plasma-based methods have also been proposed to produce high-intensity vortex beams with tilted or transverse OAM[50–52]. In this regard, it is reasonable to expect that novel nonlinear features and additional application scenarios might arise when the intensities of such STOV pulses become relativistic.

In this paper, we propose and demonstrate spatiotemporal HHG in the relativistic region driven by an intense STOV beam impinging on a solid plasma target, as shown in Figure 1(a). The red torus with wavevector k represents a linearly σ-polarized (in the z-direction) STOV pulse propagating in the $+x$-direction. It has a donut intensity distribution in the spatiotemporal plane and carries a specific TOAM, L_z. When normally reflected by an over-dense plasma target, relativistic high-order spatiotemporal harmonics are effectively generated (blue torus with k'). Using particle-in-cell (PIC) simulations, we found that the plasma surface driven by the STOV beam acts as a spatial–temporal-coupled relativistic oscillating mirror (ROM)[53–55]. Mirrors with various frequencies reflect the STOV beam and transfer spatiotemporal features to the harmonics. The topological charge and TOAM per photon of the harmonic scale with their order.

2. Simulations and results

The proposed scheme is confirmed via two-dimensional (2D) PIC simulations using the EPOCH code[56] because the spatiotemporal characteristics can be fully described in 2D spatial geometry. The near-paraxial and quasimonochromatic z-polarized STOV pulses can be expressed as follows[33,34]:

$$E_z(x,y,t) = E_0\left(\sqrt{2}\tilde{r}/w\right)^{|l|}\exp\left(-\tilde{r}^2/w^2\right)\exp\left[i\left(k_0\xi + l\tilde{\varphi}\right)\right]. \tag{1}$$

The normalized amplitude is $a_0 = eE_0/m_e c\omega_0 = 2$, where E_0 is the amplitude of the laser electric field, e and m_e are the electron charge and mass, respectively, $\omega_0 = 2\pi c/\lambda_0$ is the center frequency and $k_0 = \omega_0/c$ is the wavenumber. The spatiotemporal vortex phase is described by $l\tilde{\varphi} = l\arctan(y/\xi)$, where $\xi = x - ct$ is the spatiotemporal coupling coordinate, and $l = -1$ is the topological charge used in this study. Spatial and temporal LG-like profiles are used with $\tilde{r} = \sqrt{y^2 + \xi^2}$. The full width at half maximum (FWHM) spot size is 8 μm ($w = 4.8$ μm), and the pulse duration is $w/c =$ 16 fs. The solid target is modeled using a pre-ionized plasma with a uniform cold electron density of $n_e = 10n_c$, where $n_c = m_e\omega_0^2/4\pi e^2 \approx 1.7 \times 10^{21}$ cm^{-3} is the critical density for $\lambda_0 = 0.8$ μm. The front surface of the target is located at $x = 28$ μm, and its thickness is 2 μm. The dimensions of the simulation box are $x \times y = 36$ μm $\times$ 32 μm, with a cell size of $\mathrm{d}x \times \mathrm{d}y = (\lambda_0/128) \times (\lambda_0/128)$. Each cell contains 20 macroparticles for both the electrons and protons.

Figures 1(b)–1(d) show snapshots at $t = 101.4$ fs of the electric field E_z, frequency spectrum, intensity and TOAM density L_z for the incident STOV pulse, respectively. At this time, the beam propagated in free space and did not reach the plasma target. The field structure shown in Figure 1(b) is different from that of the conventional Gaussian beam owing to the spatiotemporal vortex phase, $\tilde{\varphi}$. At the head (beam propagating in the $+x$-direction) and tail, the phase shift of the beam from the top ($+y$) to the bottom ($-y$) is almost zero or 2π; the electric field structure is close to the Gaussian beam. However, at the center of the beam, the vortex phase results in an up-and-down phase difference of π for $l = -1$. The upper part of the field E_z has one more period than the lower part and forms a fork-shaped dislocation in the center region ($\tilde{r} \sim 0$). Thus, the frequency spectrum in Figure 1(c) splits into two parts around the center frequency, k_0, showing the polychromatic nature of the STOV pulses. The frequency chirp between the peaks of the lower-left ($0.978k_0$) and upper-right ($1.022k_0$) parts is approximately $\Delta k \sim 0.044k_0$, from which we can estimate the characteristic timescale of the temporal diffraction[33] using $ct_R = k_0/\Delta k^2 \sim 65.8$ μm, which is shorter than the spatial Rayleigh length of $x_R = \pi w^2/\lambda_0 \sim 90.5$ μm.

This field structure leads to a donut intensity distribution in the propagating xoy plane, as shown in Figure 1(d), expressed by the time-averaged energy density[29]:

$$I = \frac{1}{4}\left(\varepsilon_0|\mathbf{E}|^2 + |\mathbf{B}|^2/\mu_0\right), \tag{2}$$

where ε_0 and μ_0 are the dielectric constant and permeability of vacuum, respectively. Here, $\mathbf{E}$ and $\mathbf{B}$ are the retrieved complex-valued electromagnetic field[57]. The energy centroid of the beam is $x_0 = 14.4$ μm and $y_0 = -0.067$ μm at this moment. The energy flux can be shown by the momentum vector, $\mathbf{P}_{\mathrm{circ}} = \left(P_x - I/c, P_y\right)$ of the STOV, as indicated by the white arrows overlaid on Figure 1(d).

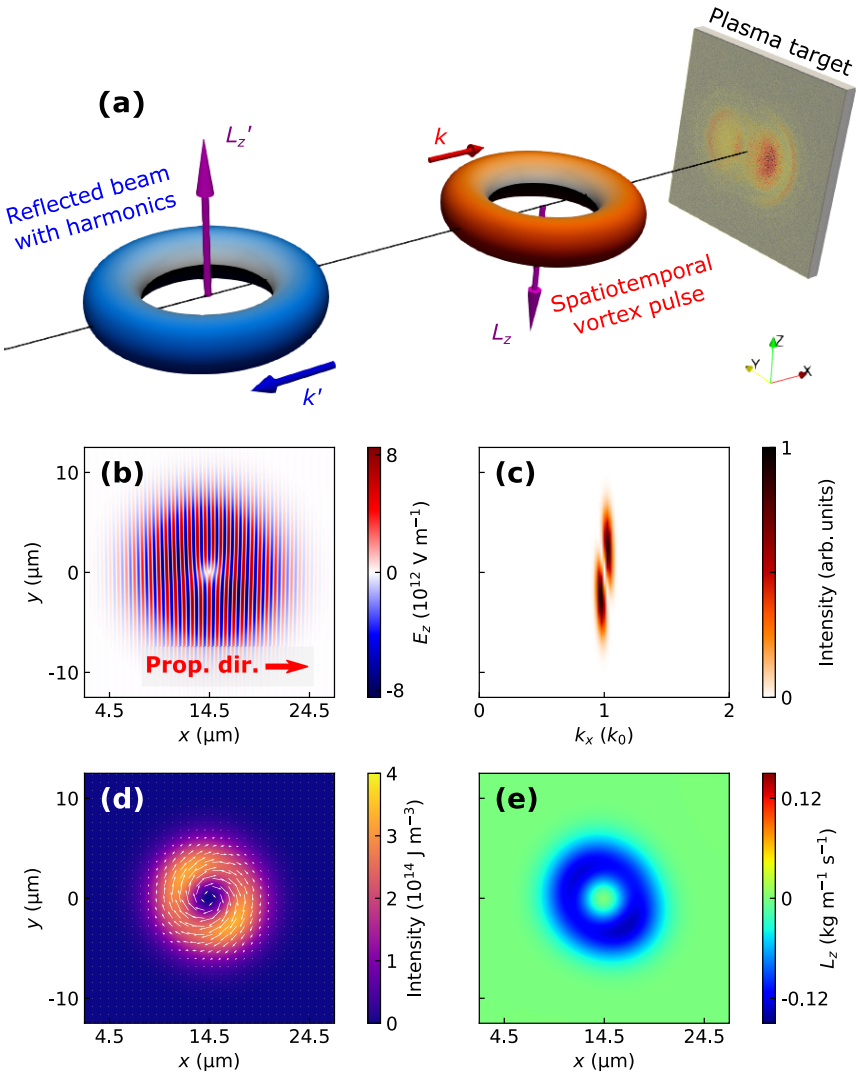

Figure 1. (a) Schematic of proposed setup. A linearly z-polarized spatiotemporal optical vortex (STOV, red torus) pulse with purely transverse orbital angular momentum (TOAM) L_z is incident onto a solid plasma target. Harmonics can be generated in the reflected beam (blue torus). (b) Snapshots of electric field E_z at $t = 101.4$ fs. (c) Frequency spectrum of (b) generated by performing Fourier transform in the x-direction. (d) Time-averaged energy density of the STOV beam. The overlaid white arrows represent the circulated momentum flux. (e) TOAM density with the subtracted propagation term. The red arrow in (b) shows the beam-propagating direction.

The energy/momentum flux circulates clockwise around the energy singularity by subtracting the propagating momentum I/c in the $+x$-direction. Here, the canonical momentum density is used to describe the momentum of the STOV beam[29]. It can be expressed as follows:

$$\mathbf{P} = \frac{1}{4\omega}\,\mathrm{Im}\left[\varepsilon_0 \mathbf{E}^* \cdot (\nabla)\,\mathbf{E} + \mathbf{B}^* \cdot (\nabla)\,\mathbf{B}/\mu_0\right]. \qquad (3)$$

The notion $\mathbf{A}^* \cdot (\nabla)\,\mathbf{A} = \sum_i A_i^* \nabla A_i$ suggests that the canonical momentum density is proportional to the local gradient of the electromagnetic field.

With the circulation of the canonical momentum, it is intuitive to calculate the TOAM of the beam using $\mathbf{L} = \mathbf{r} \times \mathbf{P}_{\mathrm{circ}}$, where $\mathbf{r}$ is the local position originating from the energy centroid. The calculated results are shown in Figure 1(e), where a purely negative TOAM is presented. By integrating in the propagating plane, we obtain a TOAM per photon of $-0.9996\hbar$ for the incident beam, corresponding to the preset topological charge of $l = -1$. The slight elliptical distribution of the intensity and TOAM in Figures 1(d) and 1(e) indicates that spatiotemporal diffraction appears.

To verify harmonic generation, we performed a 2D Fourier transform for the field at $t = 197.5$ fs when the beam was reflected entirely. The obtained high-harmonic spectra of E_z are shown in Figure 2(a), in which clear odd harmonics up till the 15th order can be observed. No evident harmonics were observed in the other electric components of E_x and E_y. The selection rules are consistent with those described by the ROM mechanism[54]. However, compared with ordinary harmonic spectra driven by a Gaussian beam, the spectral width of STOV harmonics significantly increases with the

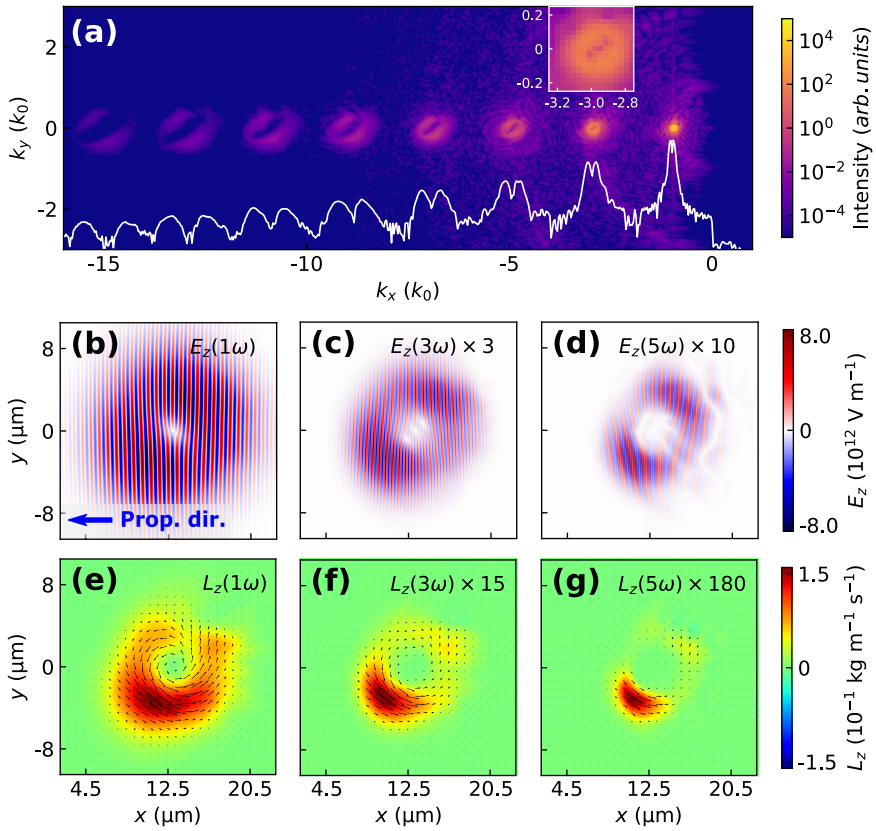

Figure 2. (a) Two-dimensional high-harmonics spectra of reflected beam E_z. The white line is a one-dimensional spectrum at $k_y = 0$. The inset in (a) shows the magnified third-harmonic spectrum region. (b)–(d) Field distributions of the (b) first, (c) third and (d) fifth harmonics. (e)–(g) TOAM densities and momentum fluxes of (b)–(d), respectively.

order, as observed by the one-dimensional spectrum in Figure 2(a) obtained at $k_y = 0$. Another significant difference is that singularities exist in the spectrum of each order, and the number is proportional to the harmonic order. As shown in the inset of Figure 2(a), three diagonally arranged singularities exist in the third-harmonic spectrum. The spatiotemporal features of the incident fundamental-frequency photons are well transferred into high-harmonic photons, owing to the conservation of the OAM under the Fourier transform[32].

Next, we extracted the fields of the first-, third- and fifth-order harmonics using the inverse Fourier transform, as shown in Figures 2(b)–2(d). The reflected fundamental-frequency beam, $E_z(1\omega)$, has a similar structure (one fork dislocation) to the incident beam but has an anticlockwise circulated momentum flux, and, accordingly, positive L_z. The TOAM per photon for $E_z(1\omega)$ was $0.95\hbar$. For the third harmonic, corresponding to its spectrum, three fork dislocations were observed. The amplitude of $E_z(3\omega)$ is approximately 2.4×10^{12} V m^{-1}, corresponding to a normalized amplitude of $a = 0.2$, which is approaching the relativistic threshold. For the fifth harmonic, the dislocations are mixed in the center region, but the upper and lower parts of $E_z(5\omega)$ differ by the five periods. The TOAMs per photon of the third and fifth harmonics are $2.67\hbar$ and $4.23\hbar$, respectively.

3. Discussion

To understand the production of spatiotemporal harmonics in detail, we studied the interaction between the STOV beam and the plasma target. According to the well-known ROM model[53–55], when an intense linearly polarized laser pulse imprints on a solid foil, the foil surface oscillates with twice the frequency of the incident pulse because the ponderomotive force it receives is $\propto 1 - \cos(2\omega t)$, where ω is the driving laser frequency. For a Gaussian pulse, $\omega = \omega_0$ is the center frequency of the entire beam. However, the frequencies of the STOV pulses are diverse at different y positions, as shown in Figure 1(c). Therefore, the oscillating frequencies of the plasma target also vary in the y-direction, which can be phenomenologically estimated by the following:

$$\left|\frac{\mathrm{d}(2\Phi)}{\mathrm{d}t}\right| = 2\omega_0 - \frac{2lc \cdot y}{(x-ct)^2 + y^2}, \tag{4}$$

where $\Phi = k_0\xi + l\varphi$ is the high-frequency oscillating phase of the STOV beam. Equation (4) clearly shows that the surface electrons in $y > 0$ ($y < 0$) oscillate at frequencies larger (less) than $2\omega_0$ for topological charge of $l = -1$.

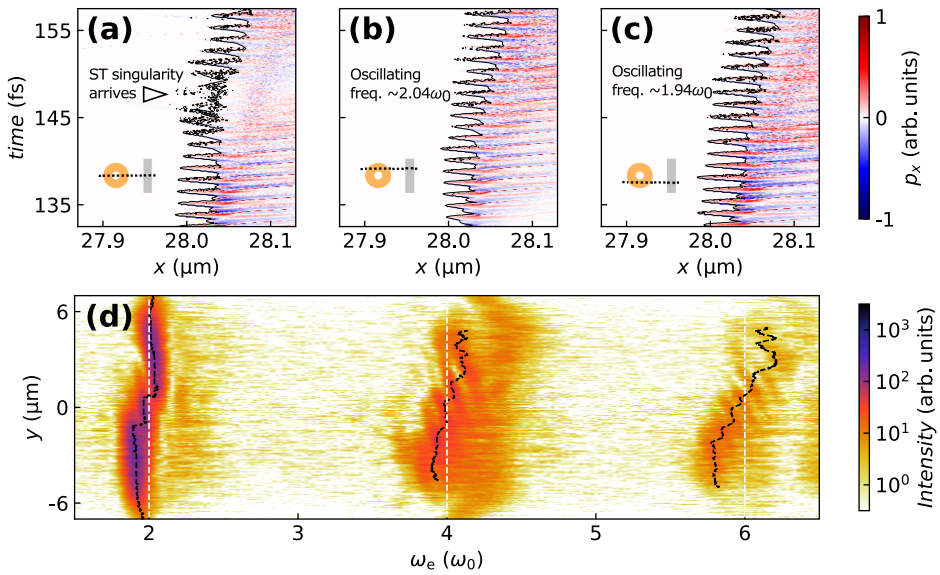

Figure 3. (a) Spatial–temporal-coupled relativistic oscillating mirror (ST-ROM). Three typical oscillating patterns are shown: (a) $y = 0$ μm, (b) $y = 2.5$ μm and (c) $y = -2.5$ μm. (d) Spectrum of the ST-ROM. The black dashed curve represents the local center angular frequency. The black line in (a)–(c) represents the density contour of $1.73n_c$ at which the beam is reflected. The spatiotemporal singularity reaches the plasma surface at approximately $t \sim 148$ fs, denoted by the triangle in (a).

In Figures 3(a)–3(c), we present three typical oscillating patterns of electron spikes at $y = 0$ and ± 2.5 μm, respectively. The black dashed lines are the contours of the electron density of γn_c at which the laser field is reflected. The relativistic Lorentz factor $\gamma = \sqrt{1 + a_0^2/2} = 1.73$ in our study ($a_0 = 2$). At $y = 2.5$ μm where the STOV beam has a higher frequency, 19 electron density spikes exist in the time range shown in Figure 3(b), corresponding to a frequency of $\sim 2.04\omega_0$. At $y = -2.5$ μm, the oscillating frequency is approximately $1.94\omega_0$. Overall, the oscillating frequency is spatial–temporally coupled, as shown by the spectrum in Figure 3(d). The plasma surface oscillates approximately at twice ($2\omega_0$) and higher even-harmonic frequencies of the driving STOV beam. These frequency-diverse spikes oscillate at almost the speed of light and reflect the STOV beam. The frequency is upshifted to orders of harmonics owing to the Doppler effect. Near the singularity with null intensity, the ponderomotive force is trivial; consequently, electron oscillation cannot be established effectively, as shown in Figure 3(a) at $t \sim 148$ fs. Therefore, harmonics are not produced at this spatiotemporal moment.

Accompanied with the electron oscillation, the STOV beam periodically exchanges TOAM with both the electrons and protons in the plasma target. The TOAM of electrons only oscillates around zero because of their instant responses to the electromagnetic field of the driving beam. However, the protons dragged by the electrons through a charge separation field accumulate a negative net TOAM. According to the conservation law of angular momentum, an immediate consequence is the loss of TOAM in the reflected beam, as shown by the TOAM densities in Figures 2(e)–2(g). In addition, this indicates that one can use a heavy-ion plasma target to mitigate TOAM losses in the spatiotemporal harmonics. Our simulation results with immobile ions confirmed that each photon carries an average TOAM of about $1.001\hbar$, $2.97\hbar$ and $4.76\hbar$ for the first, third and fifth harmonic, respectively.

The use of plasma materials resolves the damage threshold issue of normal optical media, enabling the generation of high-power EUV STOV light sources. Figure 4 shows the scaling of the TOAM per photon and the energy conversion efficiencies of the spatiotemporal harmonics driven by the STOV beam with intensities from $I_0 \approx 8.6 \times 10^{18}$ W cm^{-2} ($a_0 = 2$) to1.4×10^{20} W cm^{-2} ($a_0 = 8$). The value of TOAM per photon for each harmonic order is close and scales with the order, as shown in Figure 4(a). The conversion efficiency (Figure 4(b)) increases with increased driving pulse intensities. The power-law scaling was fitted by $I_n \propto n^{-2.99}$ for a sufficiently strong ($a_0 = 6$) STOV driver. This indicates that for the ninth-order harmonic whose center wavelength penetrates the EUV region, the energy conversion efficiency reaches 0.1%. The simulation results show that its peak intensity is approximately 3.8×10^{17} W cm^{-2}, and the TOAM per photon is approximately $6.1\hbar$. Such novel light sources may provide features beyond existing approaches for new applications.

The proposed scheme can also operate at oblique incidence, which is necessary for practical experiments. Figure 5 presents the harmonic results driven by the s-polarized STOV beam with an incident angle of $\pi/4$. Both even and odd harmonics are generated; the odd harmonics are the same s-polarized as that in the normally incident case, whereas the even harmonics are p-polarized. The presence of fork dislocations in $E_x(2\omega)$ and $E_z(3\omega)$ indicates that

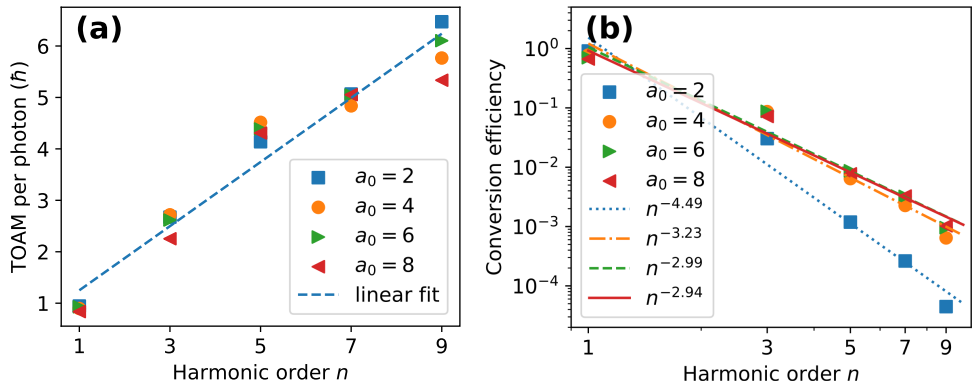

Figure 4. (a) TOAM values L_z per photon of harmonics for STOV drivers with $a_0 = 2$ (square), 4 (circle), 6 (right-hand triangle) and 8 (left-hand triangle). The blue dashed line is a linear fit of the average TOAM for each order harmonic. (b) Energy conversion efficiencies with fitted lines of the power law of harmonics.

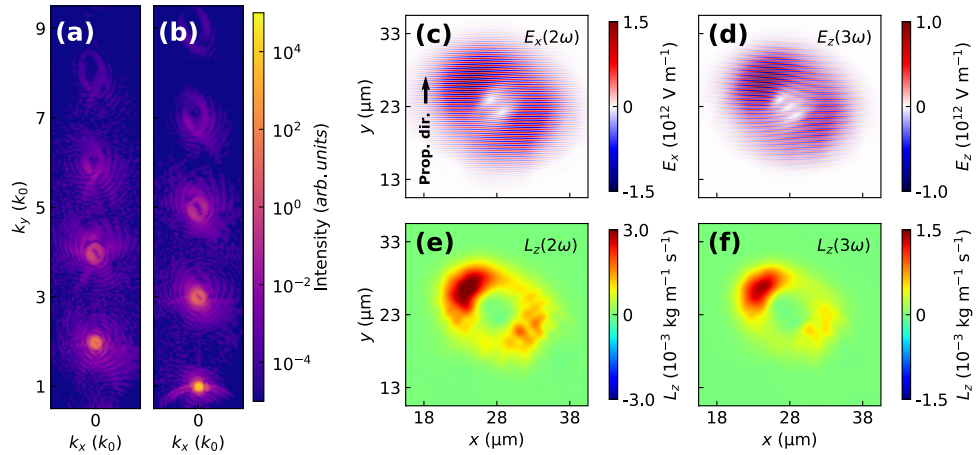

Figure 5. Spectra of (a) E_x and (b) E_z components driven by a z-polarized STOV beam with incident angle of $\pi/4$. Field distributions of the (c) second and (d) third harmonics. (e), (f) TOAM densities of (c) and (d), respectively. The reflected beam propagates in the $+y$-direction.

spatiotemporal properties are transferred to the harmonics. The TOAM per photon is $1.84\hbar$ for the second harmonic and $2.51\hbar$ for the third harmonic.

4. Conclusion

In conclusion, we have demonstrated that relativistic spatiotemporal high harmonics are generated when a high-power STOV beam carrying TOAM irradiates an overdense plasma target. The frequencies of the STOV beams are spatially diverse. Thus, it drives the spatial–temporal-coupled ROM to radiate spatiotemporal harmonics. During this process, the TOAM of the driving beam is transferred to the harmonics. Benefitting from the ultrahigh damage threshold of the plasma, the intensity of the generated harmonics approached the relativistic region. Therefore, our proposed scheme provides a promising method for producing spatiotemporal EUV vortices with extreme intensities. In addition, the direction reversal of the TOAM during the reflection suggests that it might be more efficient to deposit TOAM into the plasma than conventional longitudinal OAM. It would be interesting to examine the effects of TOAM in other relativistic STOV beam and plasma interaction scenarios.

Acknowledgements

This work was supported by the Ministry of Science and Technology of the People's Republic of China (Grant No. 2018YFA0404803), Strategic Priority Research Program of Chinese Academy of Sciences (Grant No. XDB16010000) and the National Natural Science Foundation of China (Grant Nos. 11875307, 11935008 and 11804348).

References

1. J. H. Poynting, Proc. R. Soc. London, Ser. A **82**, 560 (1909).
2. A. M. Yao and M. J. Padgett, Adv. Opt. Photon. **3**, 161 (2011).
3. L. Allen, M. W. Beijersbergen, R. J. Spreeuw, and J. P. Woerdman, Phys. Rev. A **45**, 8185 (1992).
4. M. J. Padgett, Opt. Express **25**, 11265 (2017).
5. Y. Shen, X. Wang, Z. Xie, C. Min, X. Fu, Q. Liu, M. Gong, and X. Yuan, Light Sci. Appl. **8**, 90 (2019).
6. C. N. Danson, C. Haefner, J. Bromage, T. Butcher, J.-C. F. Chanteloup, E. A. Chowdhury, A. Galvanauskas, L. A. Gizzi,

J. Hein, D. I. Hillier, N. W. Hopps, Y. Kato, E. A. Khazanov, R. Kodama, G. Korn, R. Li, Y. Li, J. Limpert, J. Ma, C. H. Nam, D. Neely, D. Papadopoulos, R. R. Penman, L. Qian, J. J. Rocca, A. A. Shaykin, C. W. Siders, C. Spindloe, S. Szatmári, R. M. G. M. Trines, J. Zhu, P. Zhu, and J. D. Zuegel, High Power Laser Sci. Eng. **7**, e54 (2019).
7. E. L. Clark, A. Grigoriadis, S. Petrakis, I. Tazes, G. Andrianaki, A. Skoulakis, Y. Orphanos, E. Kaselouris, I. Fitilis, J. Chatzakis, E. Bakarezos, V. Dimitriou, E. P. Benis, N. A. Papadogiannis, and M. Tatarakis, High Power Laser Sci. Eng. **9**, e53 (2021).
8. Y. Shi, B. Shen, L. Zhang, X. Zhang, W. Wang, and Z. Xu, Phys. Rev. Lett. **112**, 235001 (2014).
9. J. Vieira, R. M. Trines, E. P. Alves, R. A. Fonseca, J. T. Mendonca, R. Bingham, P. Norreys, and L. O. Silva, Nat. Commun. **7**, 10371 (2016).
10. A. Leblanc, A. Denoeud, L. Chopineau, G. Mennerat, P. Martin, and F. Quéré, Nat. Phys. **13**, 440 (2017).
11. C. Brabetz, S. Busold, T. Cowan, O. Deppert, D. Jahn, O. Kester, M. Roth, D. Schumacher, and V. Bagnoud, Phys. Plasmas **22**, 013105 (2015).
12. A. Denoeud, L. Chopineau, A. Leblanc, and F. Quere, Phys. Rev. Lett. **118**, 033902 (2017).
13. W. P. Wang, C. Jiang, H. Dong, X. M. Lu, J. F. Li, R. J. Xu, Y. J. Sun, L. H. Yu, Z. Guo, X. Y. Liang, Y. X. Leng, R. X. Li, and Z. Z. Xu, Phys. Rev. Lett. **125**, 034801 (2020).
14. J. Vieira and J. T. Mendonça, Phys. Rev. Lett. **112**, 215001 (2014).
15. X. M. Zhang, B. F. Shen, L. G. Zhang, J. C. Xu, X. F. Wang, W. P. Wang, L. Q. Yi, and Y. Shi, New J. Phys. **16**, 123051 (2014).
16. J. Vieira, J. T. Mendonça, and F. Quéré, Phys. Rev. Lett. **121**, 054801 (2018).
17. W. P. Wang, C. Jiang, B. F. Shen, F. Yuan, Z. M. Gan, H. Zhang, S. H. Zhai, and Z. Z. Xu, Phys. Rev. Lett. **122**, 024801 (2019).
18. Y. Shi, D. Blackman, D. Stutman, and A. Arefiev, Phys. Rev. Lett. **126**, 234801 (2021).
19. Y. Shi, D. R Blackman, and A. Arefiev, Plasma Phys. Controll. Fusion **63**, 125032 (2021).
20. Y. Shi, J. Vieira, R. M. G. M. Trines, R. Bingham, B. F. Shen, and R. J. Kingham, Phys. Rev. Lett. **121**, 145002 (2018).
21. X. Zhang, B. Shen, Y. Shi, X. Wang, L. Zhang, W. Wang, J. Xu, L. Yi, and Z. Xu, Phys. Rev. Lett. **114**, 173901 (2015).
22. X. Zhang, B. Shen, L. Zhang, and Y. Shi, High Power Laser Sci. Eng. **9**, e28 (2021).
23. J. W. Wang, M. Zepf, and S. G. Rykovanov, Nat. Commun. **10**, 5554 (2019).
24. S. Li, X. Zhang, W. Gong, Z. Bu, and B. Shen, New J. Phys. **22**, 013054 (2020).
25. C.-K. Huang, C. Zhang, Z. Nie, K. A. Marsh, C. E. Clayton, and C. Joshi, Commun. Phys. **3**, 213 (2020).
26. L. Yi, Phys. Rev. Lett. **126**, 134801 (2021).
27. L. Zhang, B. Shen, Z. Bu, X. Zhang, L. Ji, S. Huang, M. Xiriai, Z. Xu, C. Liu, and Z. Xu, Phys. Rev. Appl. **16**, 014065 (2021).
28. K. Y. Bliokh and F. Nori, Phys. Rev. A **86**, 033824 (2012).
29. K. Y. Bliokh and F. Nori, Phys. Rep. **592**, 1 (2015).
30. N. Jhajj, I. Larkin, E. W. Rosenthal, S. Zahedpour, J. K. Wahlstrand, and H. M. Milchberg, Phys. Rev. X **6**, 031037 (2016).
31. S. W. Hancock, S. Zahedpour, A. Goffin, and H. M. Milchberg, Optica **6**, 1547 (2019).
32. A. Chong, C. Wan, J. Chen, and Q. Zhan, Nat. Photon. **14**, 350 (2020).
33. K. Y. Bliokh, Phys. Rev. Lett. **126**, 243601 (2021).
34. S. W. Hancock, S. Zahedpour, and H. M. Milchberg, Phys. Rev. Lett. **127**, 193901 (2021).
35. S. Huang, P. Wang, X. Shen, and J. Liu, Opt. Express **29**, 26995 (2021).
36. J. Chen, C. Wan, A. Chong, and Q. Zhan, Nanophotonics **10**, 4489 (2021).
37. A. Mirando, Y. Zang, Q. Zhan, and A. Chong, Opt. Express **29**, 30426 (2021).
38. Q. Cao, J. Chen, K. Lu, C. Wan, A. Chong, and Q. Zhan, Sci. Bull. **67**, 133 (2021).
39. C. Wan, J. Chen, A. Chong, and Q. Zhan, Nat. Sci. Rev. **9**, nwab149 (2021).
40. H. Wang, C. Guo, W. Jin, A. Y. Song, and S. Fan, Optica **8**, 966 (2021).
41. C. Wan, J. Chen, A. Chong, and Q. Zhan, Sci. Bull. **65**, 1334 (2020).
42. M. Mazanov, D. Sugic, M. A. Alonso, F. Nori, and K. Y. Bliokh, Nanophotonics **11**, 737 (2022).
43. N. Yu, P. Genevet, M. A. Kats, F. Aieta, J. P. Tetienne, F. Capasso, and Z. Gaburro, Science **334**, 333 (2011).
44. L. Zhang, B. Shen, X. Zhang, S. Huang, Y. Shi, C. Liu, W. Wang, J. Xu, Z. Pei, and Z. Xu, Phys. Rev. Lett. **117**, 113904 (2016).
45. S. W. Hancock, S. Zahedpour, and H. M. Milchberg, Optica **8**, 594 (2021).
46. G. Gui, N. J. Brooks, H. C. Kapteyn, M. M. Murnane, and C.-T. Liao, Nat. Photon. **15**, 608 (2021).
47. Y. Fang, S. Lu, and Y. Liu, Phys. Rev. Lett. **127**, 273901 (2021).
48. J. Chen, C. Wan, A. Chong, and Q. Zhan, Opt. Express **28**, 18472 (2020).
49. G. Rui, B. Yang, X. Ying, B. Gu, Y. Cui, and Q. Zhan, Opt. Express **30**, 37314 (2022).
50. J. Qiu, B. Shen, X. Zhang, Z. Bu, L. Yi, L. Zhang, and Z. Xu, Plasma Phys. Controll. Fusion **61**, 105001 (2019).
51. Z.-Y. Chen, R. Hu, S. Zhang, and T. Yuan, Phys. Rev. A **106**, 013516 (2022).
52. W. Chen, X. Zhang, D. Xu, X. Guo, and B. Shen, Sci. Rep. **12**, 12524 (2022).
53. S. V. Bulanov, N. M. Naumova, and F. Pegoraro, Phys. Plasmas **1**, 745 (1994).
54. R. Lichters, J. Meyer-ter-Vehn, and A. Pukhov, Phys. Plasmas **3**, 3425 (1996).
55. T. Baeva, S. Gordienko, and A. Pukhov, Phys. Rev. E **74**, 046404 (2006).
56. T. D. Arber, K. Bennett, C. S. Brady, A. Lawrence-Douglas, M. G. Ramsay, N. J. Sircombe, P. Gillies, R. G. Evans, H. Schmitz, A. R. Bell, and C. P. Ridgers, Plasma Phys. Controll. Fusion **57**, 113001 (2015).
57. A. Blinne, S. Kuschel, S. Tietze, and M. Zepf, J. Comput. Phys. X **1**, 100019 (2019).